Nanoscale

High performance triboelectric nanogenerators with aligned carbon nanotubes

Huan Wang,[a] Mayue Shi,[a,b] Kai Zhu,[a] Zongming Su,[b] Xiaoliang Cheng,[b] Yu Song,[b] Xuexian Chen,[b] Zhiqiang Liao,[a] Min Zhang*[a] and Haixia Zhang*[b]

As the essential element of a triboelectric nanogenerator (TENG), friction layers play key roles that determine the device performance, which can be enhanced by material selection and surface modification. In this work, we have embedded aligned carbon nanotubes (CNTs) on the polydimethylsiloxane (PDMS) surface as the effective dielectric layer to donate electrons. This layer not only increases the electron generation for the output, but also shows notable stretchability. The length and the properties of the aligned CNTs can be controlled precisely. Using the 40 μm CNT as an example, the fabricated CNT–PDMS TENG shows an output voltage of 150 V and a current density of 60 mA m^{-2}, which are 250% and 300% enhancement compared to the TENG using directly doped PDMS/multiwall carbon nanotubes, respectively. The maximum power density of this TENG reaches 4.62 W m^{-2} at an external load of 30 MΩ. The TENG has demonstrated superior stability during cyclic measurement of over 12 000 cycles. Besides, the aligned CNT–PDMS film shows superhydrophobicity (154°) and good sheet resistance of 280 Ω sq^{-1}. This stretchable aligned CNT–PDMS film can be universally utilized as a positive triboelectric layer pairing with polymeric materials such as polyethylene terephthalate, polyimide, PDMS and polytetrafluoroethylene for TENGs. This work provides an effective method of structure design for flexible and stretchable nanogenerators.

1. Introduction

With the rapid advancement of portable and wearable electronics, energy harvesting technologies that convert light, wind, tide, and mechanical vibrations into electric energy are vitally essential to provide self-powered energy sources.[1] Most energy harvesters developed so far have relied on piezoelectric,[2–4] electromagnetic,[5] and thermoelectric effects.[6] Since 2012, a so-called triboelectric nanogenerator (TENG) has been developed to convert ambient mechanical energy into electric energy.[7] Based on the effects of triboelectrification and electrostatic induction, TENGs have promising applications in wearable electronics,[8] self-powered sensors[9,10] and wireless systems[11] with advantages of high efficiency, low cost and simple design.[12–15]

The output power of a TENG is the key to open the real industry applications. Most approaches to improve the output have focused on morphology optimization,[16] structure design,[17,18] surface modification,[19] *etc*. Only a few studies have

paid attention to the choice of materials.[20,21] Staying at the end of the tribo-series, metals such as aluminum, copper, and gold have been widely used[22–25] as the positive materials. However, these metals mainly exist in a rigid thin film form, which would reduce the charge transfer efficiency due to the non-uniform contact surface[26] and restrict their applications in stretchable and flexible devices. Thus, seeking a high performance stretchable positive material is necessary for nanogenerators. Carbon nanotubes (CNTs), which possess fascinating properties such as excellent electrical conductivity, high specific surface area, and high flexibility,[27–29] have been widely exploited in nanogenerators.[30] Besides, polydimethylsiloxane (PDMS) as a silicone elastomer with unique stretchability, biocompatibility and flexibility[31] has been widely employed in stretchable devices. Combining the advantages of these two materials leads to a promising novel positive layer. Only a few studies explored the combination of these two materials, which mainly directly mixed PDMS and multiwall carbon nanotubes (MWCNTs) together to form a composite used to fabricate a flexible TENG.[32] However, they have not obtained satisfying performance due to the limited function from the buried MWCNTs.

In this paper, we have realized the CNT–PDMS friction layer with the aligned CNTs embedded in and protruded from the PDMS, which enhances the electron generation for high

[a]School of Electronic and Computer Engineering, Peking University, Shenzhen 518055, China. E-mail: zhangm@ece.pku.edu.cn
[b]National Key Laboratory of Science and Technology on Micro/Nano Fabrication, Institute of Microelectronics, Peking University, Beijing 100871, China. E-mail: zhang-alice@pku.edu.cn

output, while it shows notable stretchability. Particularly, the material modification and the surface structure introduction can be realized simultaneously in one step with this design. By controlling the length and the property of the aligned CNTs, the performance of TENGs can be modulated and enhanced. This stretchable aligned CNT–PDMS film can be universally utilized as the positive triboelectric layer for TENGs, pairing with polymeric materials such as polyethyleneterephthalate (PET), polyimide (PI), PDMS, and polytetrafluoroethylene (PTFE).

2.   Device realization and characterization

2.1   Fabrication of the TENGs

The fabrication process is described in Fig. 1. It includes two major steps. The first is the fabrication of the aligned CNT–PDMS films, as shown in Fig. 1(a). The aligned CNTs were grown *in situ* using a plasma-enhanced chemical vapor deposition (PECVD) method, as was reported in our previous work.[33] In parallel, we used a polyethylene naphthalate (PEN) film as the transfer substrate. Two PDMS layers with a designed thickness were spin-coated on it step by step. The first layer was about 100 μm and was solidified immediately after the coating, working as the supporting base. The second PDMS layer was about 20 μm, serving as the transfer medium. After the second PDMS coating, the prepared CNT sample on the silicon substrate was inverted and plugged into the second PDMS layer. After curing of PMDS for 1 hour on a hotplate, the silicon could be gently peeled off, and the aligned CNTs were left in the PDMS film. In this process, we exploited the good wetting property of the PDMS solution on the other cured PDMS films to realize an efficient transfer. The whole film has a size of 30 mm × 30 mm as the CNT–PDMS film occupies an area of 15 mm × 10 mm. Fig. 1(c) shows that the obtained stretchable film can be easily peeled off. The CNT–PDMS film shows notable stretchability. At the same time, the film restored easily after it was stretched by 50% and maintained at the corresponding stretched position, as shown in Fig. 1(d).

After obtaining the aligned CNT–PDMS films, we began to fabricate the TENGs. Fig. 1(b) is the schematic diagram of the TENG. Starting with an indium tin oxide (ITO) coated PET film, serving as the top electrode, the friction layer of PDMS was spin-coated on it. After the PDMS is cured, the film was assembled with the prepared aligned CNT–PDMS film to form an arch-shape TENG. Fig. 1(c) shows the photographic image of the fabricated TENG, which has a size of 30 mm × 20 mm. The gap was fixed at about 3 mm.

2.2   Characterization and measurement

The morphology and structure of the aligned CNT–PDMS film were characterized using SEM (Quanta 600F, FEI Co.) and AFM (Dimension ICON, BrukerCorp). The static contact angle (CA) was measured by using a contact angle meter (DataPhysics Instruments GmbH). The TENG was driven by using a modal shaker (JZK-10) controlled by an oscilloscope (Agilent DSO-X 2014A) and an amplifier (SINOCERA YE5871A), which could provide a periodic and stable external force to the devices. The output voltage was measured *via* a digital oscilloscope (Agilent DSO-X 2014A) with a 100 MΩ probe (HP9258) directly, while the current was measured by using a load resistor of 10 kΩ.
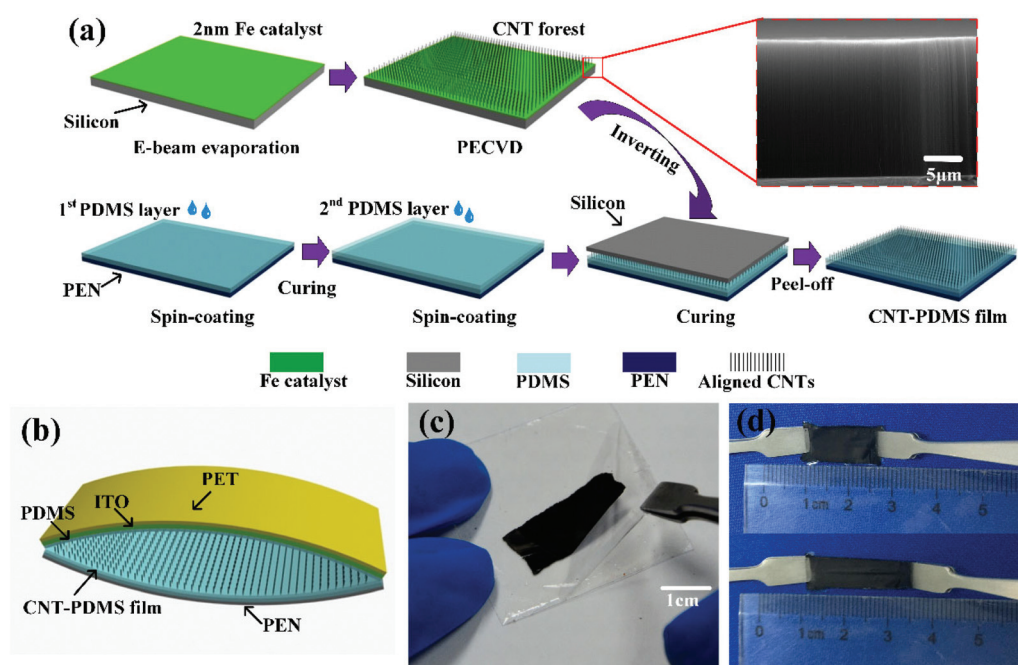

Fig. 1   (a) Schematic diagram of the process for fabricating the aligned CNT–PDMS film. (b) Schematic diagram of the TENG. (c) Photographic image of the TENG. (d) An optical image of the stretchable aligned CNT–PDMS film.

3   Results and discussion

The exposed part of the transferred CNTs should be precisely controlled to realize the output enhancement of the stretchable film in TENGs. We have investigated four series of CNT samples with different lengths for the TENGs, including 10 μm, 20 μm, 30 μm, and 40 μm. When the CNT sample was covered and plugged onto the uncured PDMS solution layer, the PDMS solution would diffuse into the CNT arrays due to the capillary wetting effect. In consequence, the PDMS solution would bond the CNTs together during the polymerization. Only a few parts of the transferred CNTs can protrude from the PDMS though the length of the as-grown CNTs is much longer than the PDMS thickness (20 μm). In Fig. 2(a), the transferred CNTs have been entirely buried inside the PDMS with the 10 μm as-grown sample, thus the film obtained a flat surface. As shown in Fig. 2(b), the PDMS has uniformly diffused into the CNT array and bonded CNTs together. The CNT–PDMS film shows a relatively flat surface with many holes inside. When adopting 30 μm and 40 μm CNT samples, the transferred CNTs protrude out, resulting in a rough surface with microstructures, as shown in Fig. 2(c) and (d), respectively.

The surface microstructures are manifolded with the length of the as-grown CNTs increasing from 10 μm to 40 μm, as shown in Fig. 3(a)–(d). The average roughness (R_a) of these stretchable films increases from 35 to 406, which means an increasing effective contact area for TENGs which can significantly enhance their output performance. These CNT–PDMS films with different CNT lengths were cut into pieces of 1 cm ∗ 1 cm, and two rigid copper rods were pressed tightly on the opposite edges of every film. Then, the sheet resistance of each film was measured by a multimeter. As shown in Fig. 3(e), the sheet resistance of these CNT–PDMS films shows
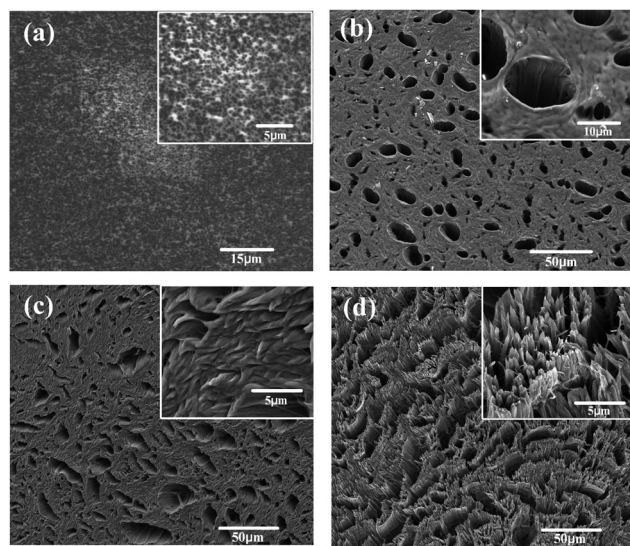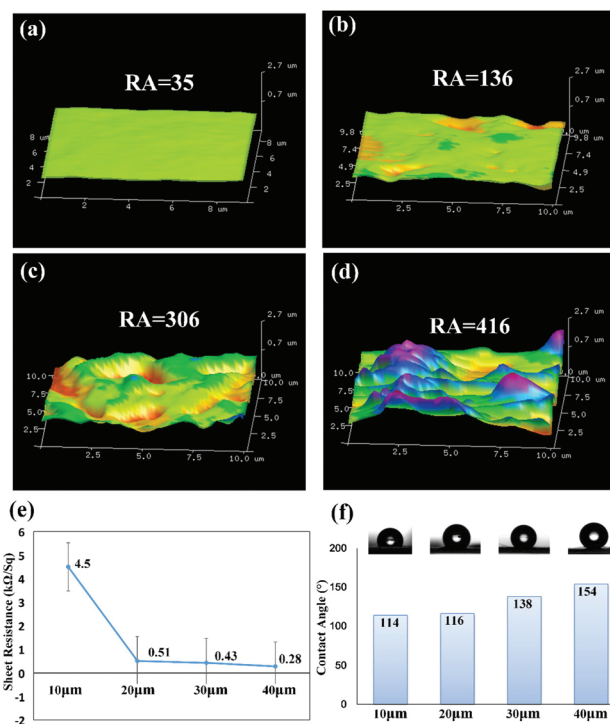

Fig. 3   Characterization of the CNT–PDMS films. AFM images of the CNT–PDMS film fabricated using the as-grown CNTs of (a) 10 μm, (b) 20 μm, (c) 30 μm and (d) 40 μm. (e) The sheet resistance and (f) static water contact angle of the CNT–PDMS films with CNTs of different lengths.

a decreasing trend as the length of the as-grown CNTs increases. The sheet resistance of the stretchable film with 10 μm CNTs was measured to be 4.5 kΩ sq^{-1}, which was much larger than those of the other films with longer CNT lengths because almost all the CNTs were buried inside the PDMS. With 40 μm as-grown CNTs, the sheet resistance of the stretchable film was measured to be 280 Ω sq^{-1}, which was 16 times smaller than that of 10 μm CNTs. Static contact angles were measured on the films of different CNT lengths with a water droplet of 5 μL, as shown in Fig. 3(f). The films with longer CNTs possess better hydrophobicity. Water droplets placed onto the films of 10 μm, 20 μm, 30 μm and 40 μm long CNTs displayed water contact angles of approximately 114°, 116°, 138°, and 154°, respectively. Among them, the film with 40 μm long CNTs shows the highest hydrophobicity or superhydrophobicity. A high surface roughness plays a key role in enhancing the hydrophobicity, which allows more air to be trapped easily underneath the water droplet so that the droplet is resisted by a thicker air layer. A relatively high water contact angle on the 40 μm CNT film is caused by both the surface roughness modulated by the CNT forest and the low surface energy imparted by the PDMS coating. The good electrical properties and superhydrophobicity of the CNT–PDMS film work together to enable its further applications in wearable and self-clean devices.

These films were then employed in TENGs, playing the dual roles as the contact surface and bottom electrode at the

Fig. 2   Top-view SEM images of the aligned CNT–PDMS films fabricated using (a) 10 μm, (b) 20 μm, (c) 30 μm and (d) 40 μm as-grown CNTs.

same time. Fig. 4(a) schematically presents the structure and basic working mechanism of the fabricated TENGs in this work. The charge generation of the TENG under an external force can be understood by the coupling of the triboelectric effect and electrostatic induction. In the initial state of the TENG, there is no charge transfer. As the CNT–PDMS film is brought into contact with the PDMS layer by applying an external force, the contact surface charges would transfer from the CNT–PDMS film electrode into the PDMS layer to bring the Fermi levels of the two materials into coincidence, resulting in the positive and the negative charges, respectively on the two surfaces. The transferred charges can be trapped in the PDMS layer for an extended period of time. When the two contacting surfaces are separated, an electrostatic potential difference is induced between the two electrodes. If the two electrodes are shorted, the electrostatic potential difference would drive electrons to flow from the ITO electrode on the top to the bottom CNT–PDMS film in order to balance the generated triboelectric potential. If an external force brings these two tribo-materials into contact again, the electrons would reversely transfer and all induced charges are neutralized.

The basic equation[34] for the conductor-to-dielectric contact-mode TENG can be expressed by

$$V = \frac{\sigma x(t)}{\varepsilon_0} - \frac{Q}{S\varepsilon_0}\left(\frac{d}{\varepsilon_r} + x(t)\right) \tag{1}$$

where ε_0, ε_r, Q and σ are the vacuum permittivity, relative permittivity of the PDMS, transferred charges between the two electrodes driven by the induced potential and triboelectric charge density on the inner surface of the PDMS. $x(t)$, d, S and t are the interlayer distance, thickness of the PDMS film, area size of the dielectrics and time, respectively. Under open-circuit (OC) conditions, there is no charge transfer so that Q is 0. Therefore, the open-circuit voltage can be derived as

$$V_{oc} = \frac{x(t)}{\varepsilon_0}\sigma. \tag{2}$$

The OC voltage is obtained at a maximum gap between the two tribo-electrification layers. From eqn (2), the output voltage (V_{oc}) is proportional to the tribo-charge surface density (σ). σ is dependent on the capacitance of the device since a contact-mode generator acts as both an energy storage and an energy output device[35] with a capacitor structure. What is more, the capacitor of the TENG can be expressed by

$$C = \frac{\varepsilon_0}{d}S\cdot\varepsilon_r. \tag{3}$$

Therefore, σ is proportional to $S\cdot\varepsilon_r$. From the equations above, the output voltage increases with an increase of S and ε_r. By embedding CNTs on the PDMS surface, the surface roughness so as the contact area has been increased. At the same time, the permittivity constant of the CNT–PDMS layer[36] has been increased. As a result, σ is increased significantly so that the performance of the TENG has been enhanced.

The directly doped PDMS/MWCNT films were then fabricated and employed in the TENGs of the same size (1 × 1.5 cm^2) for comparison, along with the 10 μm, 20 μm, 30 μm and 40 μm aligned CNT–PDMS films. They are paired with PDMS using a similar structure as shown in Fig. 1(b). Fig. 4(b) and (c) compare the electrical output performance of a directly doped PDMS/MWCNT TENG and an aligned CNT–PDMS TENG under the repeated compressive force at an applied frequency of 4 Hz. In the case of the directly doped PDMS/MWCNT TENG, the output voltage is approximately 60 V and the current density is 20 mA m^{-2}, while the aligned CNT–PDMS TENG displays an output voltage and current density of approximately 150 V and 60 mA m^{-2} under the same mechanical force, which are 2.5 and 3 times higher, respectively. The electrical output performance of the TENGs was greatly enhanced with the aligned CNTs stuck into the PDMS surface compared to the directly doped ones. Besides, TENGs using 10 μm, 20 μm, 30 μm, and 40 μm aligned CNT–PDMS films have peak voltages of 90 V, 100 V, 120 V, and 150 V, respectively, as shown in Fig. 4(d). The enhancement can be partially attributed to the introduction of the high density CNT arrays onto the film surface, which alters the surface affinity of the PDMS in a great degree. As discussed before, more transferred
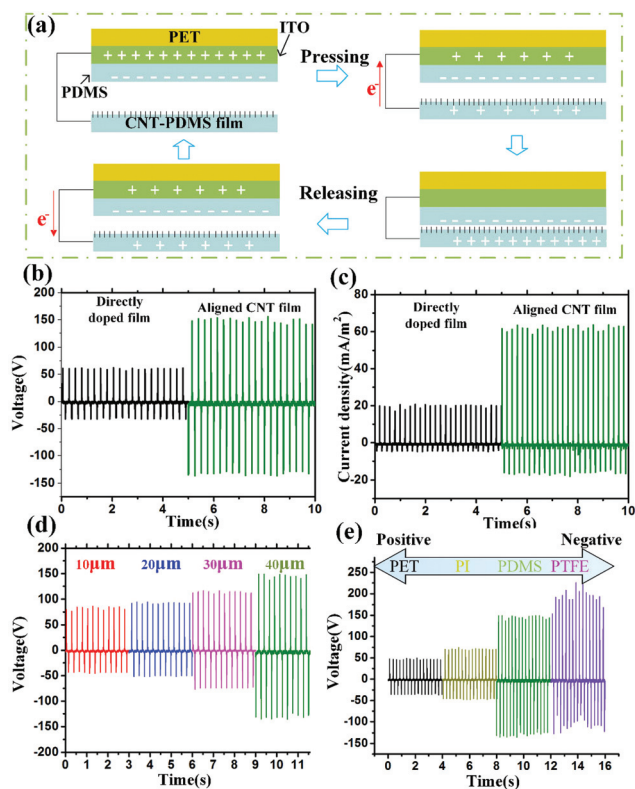
Fig. 4 (a) The operating principle of the TENG under an external force. (b) Output voltage and (c) current density comparison between the directly doped PDMS/MWCNT TENG and the aligned CNT–PDMS TENG, both with a CNT length of 40 μm. (d) Output voltages of the aligned CNT–PDMS TENGs with different CNT lengths. (e) Output voltages of the TENGs with a 40 μm aligned CNT–PDMS film paired with PET, PI, PDMS, and PTFE, respectively.

charges can be obtained with a larger affinity difference between two contact materials. Additionally, the transfer method introduces surface microstructures when using 30 μm and 40 μm as-grown CNTs, as shown in Fig. 2(c) and (d). The exposed part of the transferred CNTs bonded into bundles through the PDMS solution shows high surface roughness, which can greatly enlarge the effective contact area of the TENGs.

What is more, these stretchable aligned CNT–PDMS films show positive triboelectric polarity so that they can be universally utilized as friction materials, paired with other polymeric materials. The other three TENGs using PI, PET, and PTFE as the top friction materials instead of the PDMS were also fabricated. Fig. 4(e) shows the output voltage performance of these TENGs, which agrees well with the triboelectric series, that is, PET, PI, PDMS, and PTFE, from positive to negative.

Finally, the output voltage, current and power of the TENG with a 40 μm aligned CNT–PDMS film were measured with various external loads, as shown in Fig. 5(a) and (b). It is apparent that the output current density decreases with an increment in the resistance, while the output voltage increases gradually and reaches saturation finally. Consequently, the maximum power of the TENG reaches 4.62 W m^{-2} with an external load of 30 MΩ. Furthermore, this TENG shows good stability over 12 000 cycles at 5 Hz without obvious change in output current density, as shown in Fig. 5(c). As a practical

application, we applied the aligned CNT–PDMS TENG to drive the commercial light emitting diode (LED) lamps and charge capacitors. The TENG was connected to a capacitor or LEDs without a resistive load through a rectifier, which converts the AC pulse generated by the TENG to DC voltage. The charging graph for various capacitors is shown in Fig. 5(d). As shown in Fig. 5(e), the output power from the TENG was used to power 45 LEDs with the characters of "*MET*". In addition, Fig. 5(e) shows that single capacitors with the capacitance values of 0.68, 1, and 10 μF are charged by driving the TENG at a frequency of 5 Hz.

4. Conclusions

In conclusion, we propose and realize a high performance TENG by embedding the aligned CNTs on the PDMS surface as the effective dielectrics to donate electrons. This design introduces material modification and surface morphology at the same time. The length of the as-grown CNTs has a significant influence on the properties and performance of the obtained films, so as the TENGs. With 40 μm long CNTs, the aligned CNT–PDMS film possesses a sheet resistance of 280 Ω sq^{-1} and a contact angle of 154°. This stretchable aligned CNT–PDMS film can be universally utilized as a positive triboelectric layer, pairing with polymeric materials such as PET, PI, PDMS and PTFE for TENGs. The fabricated CNT–PDMS TENG shows an output voltage of 150 V and current density of 60 mA m^{-2}, which achieves 250% and 300% enhancement, respectively, compared with that using directly doped PDMS/MWCNTs. The maximum power density of the aligned CNT–PDMS TENG reaches 4.62 W m^{-2} at an external load of 30 MΩ. The TENG shows good stability and superior electrical performance, which is capable of driving both the instantaneous operation of 45 LEDs and the charging of capacitors. This high performance aligned CNT–PDMS based TENG shows promising potential for stretchable and biocompatible applications in wearable electronics.
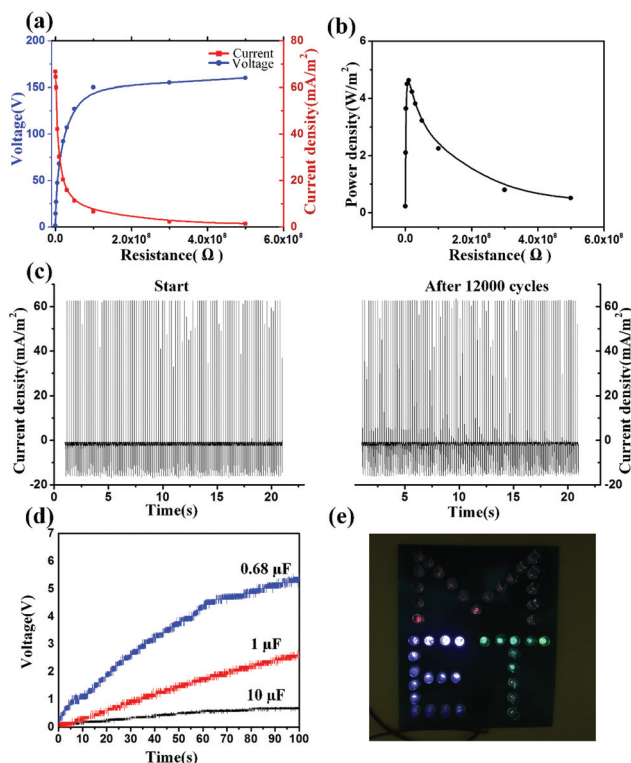
Acknowledgements

Fig. 5 (a) Output voltage, current density, and (b) power density under different external loads. (c) Electrical stability tests of the TENG for 12 000 cycles. (d) Charging graph of various capacitors. (e) The TENG was employed as a direct power source for an LED array with the characters of "MET".

Notes and references

1 Z. L. Wang, *ACS Nano*, 2013, 7, 9533–9557.
2 M. D. Han, X. X. Chen, Y. B. Cheng and H. X. Zhang, *Adv. Electron. Mater.*, 2015, 1500187.

3 B. J. Hansen, Y. Liu, R. Yang and Z. L. Wang, *ACS Nano*, 2010, **4**, 3647–3652.

4 N. Wu, X. Cheng, Q. Zhong, J. Zhong, W. Li, B. Wang, B. Hu and J. Zhou, *Adv. Funct. Mater.*, 2015, **25**, 4788–4794.

5 S. P. Beeby, R. N. Torah, M. J. Tudor, P. Glynne-Jones, T. O'Donnell, C. R. Saha and S. Roy, *J. Micromech. Microeng.*, 2007, **17**, 1257–1265.

6 S. J. Kim, J. H. We and B. J. Cho, *Energy Environ. Sci.*, 2014, **7**, 1959.

7 F. R. Fan, Z. Q. Tian and Z. L. Wang, *Nano Energy*, 2012, **1**, 328.

8 M. Y. Shi, J. X. Zhang, H. T. Chen, M. D. Han, S. Gowda, Z. M. Su, B. Meng, X. L. Cheng and H. X. Zhang, *ACS Nano*, 2016, **10**, 4083–4091.

9 J. Zhong, H. Zhu, Q. Zhong, J. Dai, W. Li, S. Jang, Y. Yao, D. Henderson, Q. Hu, L. Hu and J. Zhou, *ACS Nano*, 2015, **9**, 7399–7406.

10 X. L. Cheng, Y. Song, M. D. Han, B. Meng, Z. M. Su, L. M. Miao and H. X. Zhang, *Sens. Actuators*, 2016, **247**, 206–214.

11 S. Wang, L. Lin and Z. L. Wang, *Nano Lett.*, 2012, **12**, 6339–6346.

12 X. S. Zhang, M. D. Han, R. X. Wang, F. Y. Zhu, Z. H. Li, W. Wang and H. X. Zhang, *Nano Lett.*, 2013, **13**, 1168–1172.

13 X. L. Cheng, B. Meng, X. X. Chen, H. T. Chen, Z. M. Su, M. Y. Shi and H. X. Zhang, *Small*, 2016, **12**, 229–236.

14 B. Meng, W. Tang, X. S. Zhang, M. D. Han, W. Liu and H. X. Zhang, *Nano Energy*, 2013, **2**, 1101–1106.

15 X. S. Zhang, M. D. Han, B. Meng and H. X. Zhang, *Nano Energy*, 2015, **11**, 304–322.

16 S. Lee, W. Ko, Y. Oh, J. Lee, G. Baek, Y. Lee, J. Sohn, S. Cha, J. Kim, J. Park and J. Hong, *Nano Energy*, 2015, **12**, 410–418.

17 M. D. Han, X. S. Zhang, B. Meng, W. Liu, W. Tang, X. M. Sun, W. Wang and H. X. Zhang, *ACS Nano*, 2013, **7**, 8554–8560.

18 B. Meng, W. Tang, Z. H. Too, X. S. Zhang, M. D. Han and H. X. Zhang, *Energy Environ. Sci.*, 2013, **6**, 3235–3240.

19 X. S. Zhang, M. D. Han, R. X. Wang, B. Meng, F. Y. Zhu, X. M. Sun, W. Wang, Z. H. Li and H. X. Zhang, *Nano Energy*, 2014, **4**, 123–131.

20 X. S. Zhang, J. Brugger and B. Kim, *Nano Energy*, 2016, **20**, 37–47.

21 J. Chen, H. Y. Guo, X. M. He, G. L. Liu, Y. Xi and H. F. Shi, *ACS Appl. Mater. Interfaces*, 2015, **8**, 736–744.

22 W. Tang, T. Jiang, F. R. Fan, A. F. Yu, C. Zhang, X. Cao and Z. L. Wang, *Adv. Funct. Mater.*, 2015, **25**, 3718–3725.

23 S. Niu and Z. L. Wang, *Nano Energy*, 2015, **14**, 161–192.

24 G. L. Qiu, W. Liu, M. D. Han, X. L. Cheng, B. Meng, A. S. Smitha, J. M. Zhao and H. X. Zhang, *Sci. China: Technol. Sci.*, 2015, **58**, 842–847.

25 D. Kim, S. J. Park, S. B. Jeon, M. L. Seol and Y. K. Choi, *Adv. Electron. Mater.*, 2016, **2**, 1500331.

26 K. N. Kim, Y. K. Jung, J. Chun, B. U. Ye, M. Gu, E. Seo, S. Kim, S. W. Kim, B. S. Kim and J. M. Baik, *Nano Energy*, 2016, **26**, 360–370.

27 M. F. L. De Volder, S. H. Tawfick, R. H. Baughman and A. John Hart, *Science*, 2013, **339**, 535–539.

28 M. M. J. Treacy, T. W. Ebbesen and J. M. Gibson, *Nature*, 1996, **381**, 678–680.

29 G. Gruner, *J. Mater. Chem.*, 2006, **16**, 3533–3539.

30 J. W. Zhong, Y. Zhang, Q. Z. Zhong, Q. Y. Hu, B. Hu, Z. L. Wang and J. Zhou, *ACS Nano*, 2014, **8**, 6273–6280.

31 A. Mata, A. J. Fleischman and S. Roy, *Biomed. Microdevices*, 2005, **7**, 281–293.

32 Y. B. Zhu, B. Yang, J. Q. Liu, X. Z. Wang, L. X. Wang, X. Chen and C. S. Yang, *Sci. Rep.*, 2016, **6**, 22233.

33 H. Wang, M. Y. Shi, K. Zhu, Z. M. Su, M. Zhang and H. X. Zhang, The 11th Annual IEEE International Conference on Nano/Micro Engineered and Molecular Systems, 2016.

34 S. Niu, S. H. Wang, L. Lin, Y. Liu, Y. S. Zhou, Y. F. Hu and Z. L. Wang, *Energy Environ. Sci.*, 2013, **6**, 3576–3583.

35 X. M. He, H. Y. Guo, X. L. Yue, J. Gao, Y. Xi and C. G. Hu, *Nanoscale*, 2015, **7**, 1896–1903.

36 L. J. Romasanta, M. Hernández, M. A. López-Manchado and R. Verdejo, *Nanoscale Res. Lett.*, 2011, **6**, 1.